

Time-domain upconversion measurements of group-velocity dispersion in quantum cascade lasers

Hyunyong Choi,¹ Laurent Diehl,² Federico Capasso², David Bour^{3,4},
Scott Corzine^{3,5}, Jintian Zhu³, Gloria Höfler^{3,6} and Theodore B.
Norris^{1,*}

¹Center for Ultrafast Optical Science, Department of Electrical Engineering and Computer Science, University of Michigan, Ann Arbor, Michigan 48109-2099, USA

²School of Engineering and Applied Sciences, Harvard University, Cambridge, Massachusetts 02138, USA

³Agilent Laboratories, 3500 Deer Creek Road, Palo Alto, California 94304, USA

⁴Bridgelux Inc, 1225 Bordeaux Dr, Sunnyvale, California 94089, USA

⁵Infinera HQ, 169 Java Dr, Sunnyvale, California 94089, USA

⁶Argos Tech LLC, 3671 Enochs St, Santa Clara, California 95051, USA

*Corresponding author: tnorris@eecs.umich.edu

Abstract: A time-resolved mid-infrared upconversion technique based on sum-frequency generation was applied to measure pulse propagation in $\lambda \sim 5.0 \mu\text{m}$ quantum cascade lasers operated in continuous wave at 30 K. The wavelength-dependent propagation delay of femtosecond mid-infrared pulses was measured to determine the total group-velocity dispersion. The material and waveguide dispersion were calculated and their contributions to the total group-velocity dispersion were found to be relatively small and constant. The small-signal gain dispersion was estimated from a measurement of the electroluminescence spectrum without a laser cavity, and was found to be the largest component of the total GVD. A negative group-velocity dispersion of β_2 ($=d^2\beta/d\omega^2$) approximately $-4.6 \times 10^{-6} \text{ ps}^2/\mu\text{m}$ was observed at the peak emission wavelength, and good agreement was found for the measured and calculated pulse-broadening.

© 2007 Optical Society of America

OCIS codes: (140.5965) Semiconductor lasers, quantum cascade; 320.7100 Ultrafast measurements

References and links

1. G. P. Agrawal, "Effect of Gain Dispersion on Ultrashort Pulse Amplification," *IEEE J. Quantum Electron.* **27**, 1843–1849 (1991).
2. H. A. Haus and Y. Silberberg, "Laser Mode Locking with Addition of Nonlinear Index," *IEEE J. Quantum Electron.* **QE-22**, 1048–1060 (1986).
3. W. Lu, L. Yan and C. R. Menyuk, "Dispersion Effects in an Actively Mode-Locked Inhomogeneously Broadened Laser," *IEEE J. Quantum Electron.* **QE-22**, 1317–1324 (2002).
4. R. Paiella, F. Capasso, C. Gmachl, and H. Y. Hwang, D. L. Svico, A. L. Hutchinson, A. Y. Cho and H. C. Liu, "Monolithic Active Mode Locking of Quantum Cascade Lasers," *Appl. Phys. Lett.* **77**, 169–171 (2000).

5. A. Soibel and F. Capasso and C. Gmachl and M. L. Peabody and A. M. Sergent and R. Paiella and H. Y. Hwang and D. L. Sivco and A. Y. Cho and H. C. Liu and C. Jirauschek and F. X. Kärtner, "Active Mode Locking of Broadband Quantum Cascade Lasers," *IEEE J. Quantum Electron.* **40**, 844–851 (2004).
6. R. Paiella and F. Capasso and C. Gmachl and D. L. Sivco and J. N. Bailargeon and A. L. Hutchinson and A. Y. Cho, "Self-Mode-locking of Quantum Cascade Lasers with Giant Ultrafast Optical Nonlinearities," *Science* **290**, 1739–1742 (2000).
7. C. Y. Wang and L. Diehl and A. Gordon and C. Jirauschek and F. X. Kärtner and A. Belyanin and D. Bour and S. Corzine and G. Hofler and M. Troccoli and J. Faist and F. Capasso, "Coherent Instabilities in a Semiconductor Laser with Fast Gain Recovery," *Phys. Rev. A* **75**, 031802-1–031802-4 (2007).
8. D. Hofstetter and J. Faist, "Measurement of Semiconductor Laser Gain and Dispersion Curves Utilizing Fourier Transforms of the Emission Spectra," *IEEE Photon. Technol. Lett.* **11**, 1372–1374 (1999).
9. C. Gmachl and A. Straub and R. Colombelli and D. L. Sivco and F. Capasso and A. Y. Cho, "Minimal Group Refractive Index Dispersion and Gain Evolution in Ultra-Broad-Band Quantum Cascade Lasers," *IEEE Photon. Technol. Lett.* **14**, 1671–1673 (2002).
10. J. Shah, "Ultrafast Luminescence Spectroscopy Using Sum Frequency Generation," *IEEE J. Quantum Electron.* **24**, 276–288 (1988).
11. M. P. Kesler and E. P. Ippen, "Femtosecond Time-Domain Measurements of Group Velocity Dispersion in Al-GaAs Diode Lasers," *Electron. Lett.* **25**, 640–642 (1989).
12. M. P. Kesler and E. P. Ippen, "Femtosecond Time-Domain Measurements of Group Velocity Dispersion in Diode Lasers at $1.5\mu\text{m}$," *IEEE J. Lightwave Technol.* **10**, 616–619 (1992).
13. R. Gordon and A. P. Heberle and J. R. A. Cleaver, "Measuring the Above-Threshold Group-Velocity Dispersion and Gain Curvature of a Semiconductor Laser by Pulse-Propagation Techniques," *J. Opt. Soc. Am. B* **21**, 29–35 (1994).
14. L. Diehl and D. Bour and S. Corzine and J. Zhu and G. Höfler and B. G. Lee and C. Y. Wang and M. Troccoli and F. Capasso, "Pulsed- and Continuous-Mode Operation at High Temperature of Strained Quantum-Cascade Lasers Grown by Metalorganic Vapor Phase Epitaxy," *Appl. Phys. Lett.* **88**, 2011151–20111515 (2006).
15. L. Diehl and D. Bour and S. Corzine and J. Zhu and G. Höfler and M. Lončar and M. Troccoli and F. Capasso, "High-Power Quantum Cascade Lasers Grown by Low-Pressure Metal Organic Vapor-Phase Epitaxy Operating Continuous Wave Above 400 K," *Appl. Phys. Lett.* **88**, 0411021–0411023 (2006).
16. E. D. Palik, *Handbook of optical constants of solids*, (Academic Press, New York, 1985).
17. R. Maulini and M. Beck and J. Faist and E. Gini, "Broadband tuning of external cavity bound-to-continuum quantum-cascade lasers," *Appl. Phys. Lett.* **84**, 1659–1661 (2004).
18. A. Yariv, *Quantum Electronics*, (WILEY, New York, 1989).
19. A. Siegman, *Lasers*, (University Science Books, Sausalito, California, 1986).

1. Introduction

Group-velocity dispersion (GVD) in semiconductor lasers is critical for understanding ultra-short pulse generation and propagation [1]. For stable pulse generation, the sign of the GVD should be opposite that of the optical nonlinearity in the host medium [2, 3]. Quantum cascade lasers (QCL's) are particularly interesting devices since the optical Kerr nonlinearity and the associated gain dispersion are embedded in a single semiconductor structure and they both originate from the same physical mechanism, i.e. the optical intersubband transition. There has been some work on ultrashort pulse generation in QCL's [4, 5], which has indicated that few-picosecond-long short pulses can be generated by active mode-locking, and evidence of passive mode-locking has been observed [6], although the nature of pulse generation in QCL's and the effects of coherent instabilities [7] remain active areas of research today. For understanding the dynamics of QCL's including pulse generation, it is important to understand quantitatively the separate contributions of the material, waveguide, and gain dispersion to the total GVD in QCL waveguide structures.

To date, the dispersion analysis of QCL's has mostly relied on DC measurement techniques: Fabry-Pérot spectrum analysis or Hakki-Paoli gain measurement for the gain dispersion [8, 9]. However, in order to take into account the dynamical interaction between the propagating pulses and the gain medium, it is more useful to investigate the effects of the GVD on the propagating pulses directly in the time domain.

In this paper, we present a simple time-domain measurement of GVD employing an ultrafast

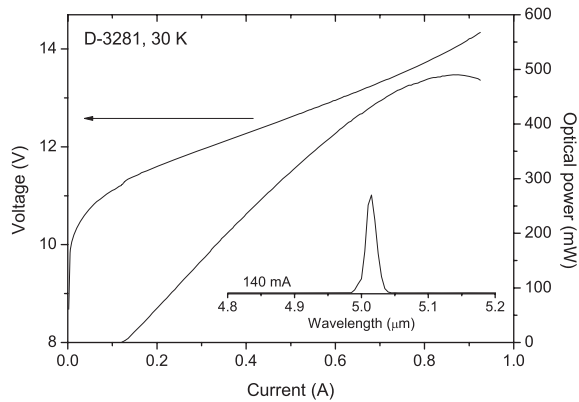


Fig. 1. CW L-I-V characteristics of the D3281 QCL at 30 K. Inset: lasing spectrum ($\sim 5 \mu\text{m}$) at the bias current of 0.14 A. Note that all the upconversion experiments for the GVD have been done below threshold (0.12 A at 30K) to prevent the device's self-heating and also to minimize the optical feedback effect.

optical technique based on sum-frequency generation [10]. Our approach is to inject femtosecond tunable mid-infrared (IR) pulses into QCL active waveguide structures and time-resolve the transmitted pulses for different peak wavelengths of the injected pulses. The experiments presented here are analogous to a number of experiments on bipolar interband semiconductor diode lasers [11, 12, 13]. In contrast to those measurements, we explicitly consider the contribution of the small-signal gain dispersion, which is obtained through an independent electroluminescence measurement of the gain spectrum. We also present detailed simulation results for the material and waveguide dispersion. The calculated material and waveguide dispersion with the independently measured gain dispersion are then used to model the effects of total GVD on the temporal pulse broadening and are compared with experimental measurements, thus providing a self-consistent picture of the effects of the GVD on the propagation of resonant mid-IR pulses.

2. QCL characteristics and time-resolved upconversion measurements

The active region of the $\sim 5 \mu\text{m}$ QCL (D3281) used in the present experiment is based on a so-called "bound-to-continuum" design grown by metal organic vapor-phase epitaxy (MOVPE). The strained $\text{In}_{0.6}\text{Ga}_{0.4}\text{As}/\text{In}_{0.44}\text{Al}_{0.56}\text{As}$ layers were deposited at a slow rate (0.1 nm/s) and the doping in the injector region was kept low to limit the waveguide losses. The waveguide consists of two low-doped InGaAs layers (300 nm thick, doping $3 \times 10^{16} \text{ cm}^{-3}$) and two InP cladding layers (3 μm thick, doping $1 \times 10^{17} \text{ cm}^{-3}$) surrounding the 30 QCL stacks composing the waveguide core. A highly-doped InP cap layer (0.5 μm thick, doping $1 \times 10^{19} \text{ cm}^{-3}$) was grown to decouple the optical mode from the lossy metal contacts. A detailed discussion of this structure and its performance can be found in Ref. [14]. The device used in our experiment was a buried heterostructure laser with Fe-doped InP regrown on the side of the ridge (see for example Ref. [15] for details on the processing). The ridge width of the QCL studied was 7.5 μm and its length was 3.795 mm long. Figure 1 shows the voltage and the optical power vs. current characteristics (L-I-V) measured at 30 K in continuous mode (CW). The threshold current density and the slope efficiency were equal to 0.44 kA/cm^2 and close to 0.8 W/A respectively at this temperature.

A schematic of an ultrafast upconversion experiment setup is shown in Fig. 2. Tunable mid-IR pulses of approximately 200-fs duration were generated using a tunable optical paramet-

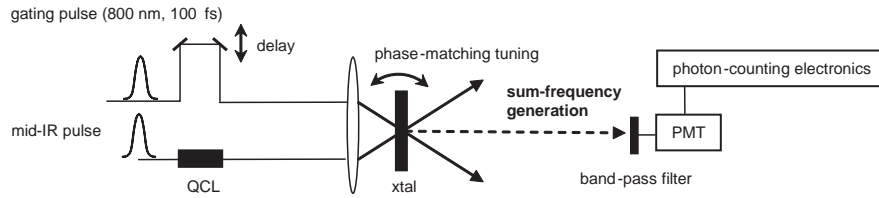


Fig. 2. Experimental setup for the GVD measurements in a QCL. Transmitted mid-IR pulse is upconverted with 800-nm pulse to detect the sum frequency photon.

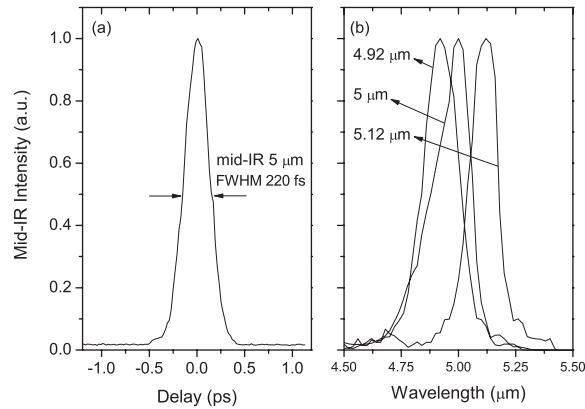


Fig. 3. (a) Typical cross-correlation trace of mid-IR pulse at $5 \mu\text{m}$, showing the intensity FWHM of ~ 220 fs. (b) Spectrally tunable mid-IR pulses are used to measure the mid-IR peak wavelength dependent pulse transit time.

ric amplifier (OPA) and difference frequency generator (DFG) pumped by a 100-fs, 250-kHz Ti:sapphire regenerative amplifier. The peak wavelength of the mid-IR pulses was continuously tunable from 3 to $7 \mu\text{m}$ with nearly transform-limited pulse shape. The mid-IR pulses were characterized by intensity cross-correlation with variably-delayed 100-fs 800 nm pulses from the Ti:sapphire amplifier by sum frequency generation, as shown in Fig. 3. The mid-IR pulses were coupled through one facet of a QCL waveguide and the output from the other facet was upconverted with the delayed 100-fs 800 nm pulses in an angle-phase-matched nonlinear crystal (KTA); the sum frequency was selected with a 10-nm band-pass filter and detected with a GaAsP photomultiplier (Hamamatsu H7421-40) and photon-counting electronics. This non-degenerate, non-collinear upconversion scheme provided a large spatial and spectral dynamic range, since the upconverted photons are spatially and spectrally well separated from the mid-IR and 800-nm beams.

For the time-domain GVD measurements, the transmitted mid-IR pulses through the QCL were measured for different peak wavelengths of the injected mid-IR pulses, and the arrival delay at each pulse was time-resolved. In Fig. 4, a typical upconversion trace is displayed for the QCL biased at 0.12 A (below threshold). A significant fraction of the incident mid-IR pulse energy was not coupled into the waveguide, and this was used as a reference time delay, i.e. the zero-time delay in the time-resolved scans of Fig. 4(b). The light coupled into the waveguide mode can be observed for many round trips if the QCL is biased near or above threshold, which enabled the coupling into the waveguide to be optimized in a straightforward way. The propagation delay for pulses coupled into the waveguide was measured relative to the uncoupled component as a function of the center wavelength of the mid-IR pulses. As seen

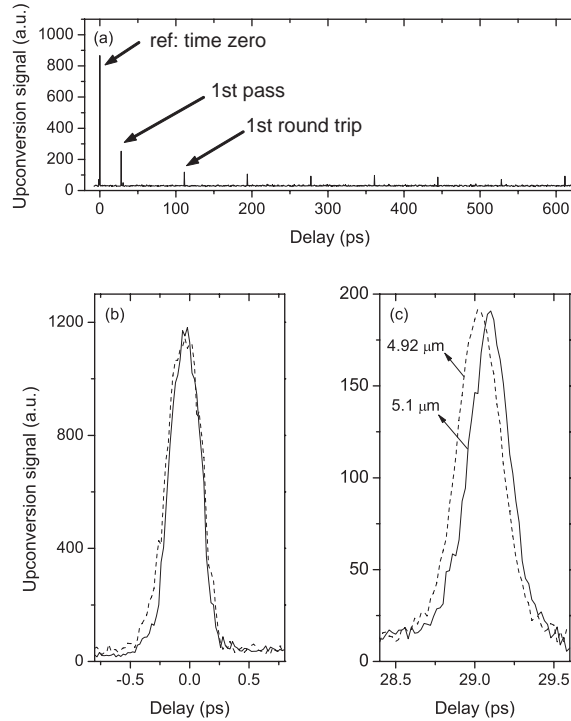


Fig. 4. (a) An example of a time-resolved upconversion trace is displayed for a QCL bias current of 0.12 A. (b) The upconversion signal at the reference time delay, i.e. time-zero delay, is shown for center wavelengths 4.92 μm (dashed) and 5.12 μm (solid). (c) Upconversion signals for two different center wavelengths are shown, illustrating the shift in pulse group delay with wavelength.

in Fig. 4(c), the wavelength-dependent propagation delays clearly show the dispersive nature of the QCL active waveguide, and indicate the total dispersion is in an anomalous dispersion regime; the blue travels faster than the red. The experimentally measured propagation delays and pulse broadening as a function of the center wavelength of the injected mid-IR pulses are summarized in Fig. 5.

In the following discussion, the group index n_g is determined from

$$\tau_{delay} = \frac{L}{v_g} = \frac{L}{c} n_g \quad (1)$$

where τ_{delay} is the group delay of the mid-IR pulse, v_g is the group velocity of the pulse, L is the length of the QCL and c is the speed of light in vacuum. The wavelength dependent group-index dispersion $dn_g/d\lambda$ is expressed as

$$\frac{dn_g}{d\lambda} = \frac{c}{L} \frac{d\tau_{delay}}{d\lambda} \quad (2)$$

which is directly related to the experimentally measured values as shown in Fig. 5(a).

The commonly used GVD parameter $\beta_2 (=d^2\beta/d\omega^2)$, which determines the pulse broadening, can be expressed as

$$\beta_2 = \frac{d^2\beta}{d\omega^2} = \frac{d\lambda}{d\omega} \frac{d}{d\lambda} \left(\frac{1}{v_g} \right) = -\frac{\lambda^2}{2\pi c L} \frac{d\tau_{delay}}{d\lambda} \quad (3)$$

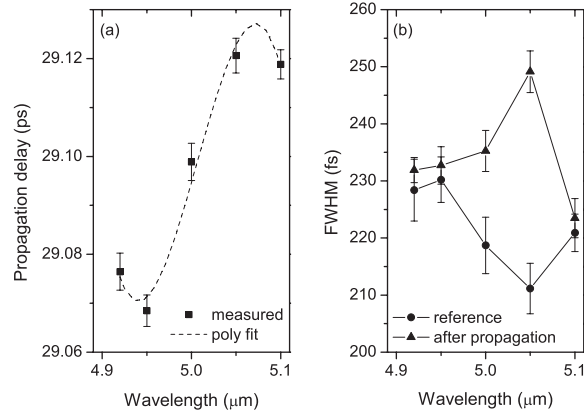


Fig. 5. (a) The measured propagation delays (filled squares) are displayed as a function of the peak wavelength of the injected mid-IR pulse. A third-order polynomial fit (dashed line) to the measured delays is used to calculate GVD parameter β_2 via Eqs. 2-3. (b) Assuming the mid-IR pulse as a Gaussian, the intensity FWHM of reference pulses (filled circles) and that of transmitted mid-IR pulses (filled upper triangles) are shown as a function of wavelength. The error bars from the chi-squared determined errors ($\sim \pm 5$ fs) are due to the long-term intensity fluctuation of our femtosecond laser sources.

Therefore, the experimentally measured propagation delays of Fig. 5(a) are directly related to the total GVD parameter β_2 via Eq. 3.

In general, the total dispersion of an active waveguide consists of three separate contributions: material, waveguide, and gain dispersion. In the following few sections, we consider each dispersion contribution in turn. In this case, the group velocity v_g and the GVD parameter β_2 are related to the index dispersion by

$$v_g = c \left(n - \lambda \frac{dn}{d\lambda} \right)^{-1} \quad (4)$$

$$\beta_2 = \frac{d^2\beta}{d\omega^2} = \frac{d\lambda}{d\omega} \frac{d}{d\lambda} \left(\frac{1}{v_g} \right) = \frac{\lambda^3}{2\pi c^2} \frac{d^2n}{d\lambda^2} \quad (5)$$

3. Material and waveguide dispersion

In order to determine the contributions of both the material and the waveguide dispersion to the group-index dispersion, we used the commercial software COMSOL Multiphysics to compute the effective refractive index of the TM_{00} mode of the laser. The restriction to this particular mode is due to the fact that the coupling of the mid-IR pulse generated by our laser system into the TM_{01} mode of the QCL waveguide is negligible due to symmetry. The refractive index of the different bulk layers composing the QCL waveguide was taken from Ref. [16] and the effect of the doping was included using the Drude model [16]. The refractive index of the gain medium was calculated by a proper weighted average of the refractive index of InAs, AlAs and GaAs. The Drude model was also used in that case to determine the effect of doping in the injector, assuming that the carriers are homogeneously distributed among the InGaAs quantum wells only.

The change of the refractive index with temperature was taken into account by using the linear coefficients $dn/dT=1.6 \times 10^{-4} \text{ K}^{-1}$ for InP layers and $0.45 \times 10^{-4} \text{ K}^{-1}$ for the ternary alloys [16]. The temperature across the device was assumed to be constant and equal to the

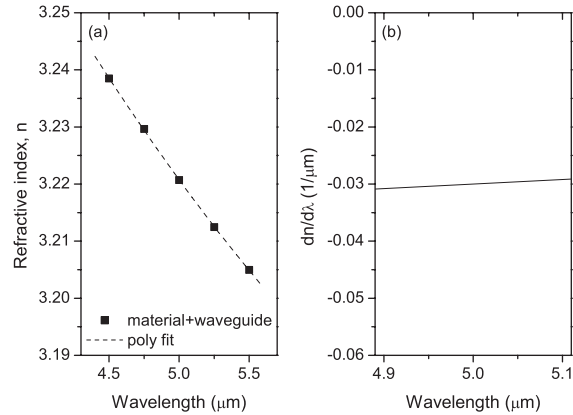


Fig. 6. (a) Effective refractive index vs. wavelength curve. The dashed line is a polynomial fit of the calculated discrete points. (b) The corresponding refractive index dispersion $dn/d\lambda$ is shown as a function of wavelength.

submount temperature (30 K). This simplification is reasonable given the low CW electrical power used to drive the sample and the low thermal resistance of buried heterostructure lasers.

Fig. 6 show the result of our 2D mode calculations. In our model, the waveguide losses are equal to 2.28 cm^{-1} at $\lambda = 5 \mu\text{m}$. The dependence of the effective refractive index on the wavelength can be approximated accurately by a quadratic fit: $n_{\text{eff}}(\lambda) \simeq 0.004\lambda^2 - 0.07\lambda + 3.48$ and the corresponding index dispersion $dn/d\lambda$ is then $\simeq 0.008\lambda - 0.07$.

The contributions from the waveguide and the material dispersion are interdependent and therefore difficult to separate exactly. However it is clear that the material dispersion can account for only part of the difference $\Delta n_{\text{eff}} = -0.033$ found as the wavelength varies from 4.5 to $5.5 \mu\text{m}$. Indeed the refractive index of the different layers composing the waveguide changes by -0.018 at most in this wavelength range. The effect of the waveguide dispersion therefore has to be important. The TM_{00} mode overlaps mostly with the gain medium (0.63 at $\sim 5.0 \mu\text{m}$), the InP cladding layers (0.20 at $\sim 5.0 \mu\text{m}$) and the bulk InGaAs layers (0.14 at $\sim 5.0 \mu\text{m}$). Our calculations show that the main contributions to the waveguide dispersion come from the overlap with the first two waveguide layers mentioned above. It changes significantly between 4.5 to $5.5 \mu\text{m}$, from 0.67 to 0.59 in the case of the active medium and from 0.16 to 0.22 in the case of the InP cladding layers, supporting the statement that the waveguide dispersion plays a non-negligible role in the index dispersion.

4. Gain dispersion

In order to estimate the contribution of the small-signal gain dispersion, i.e. excluding the effects of the optical feedback and gain narrowing, we processed a section of wafer D3281 into a mesa structure and independently measured the electroluminescence spectrum. As shown in Fig. 7, the measured FWHM of the electroluminescence spectrum at 30 K was $\sim 18 \text{ meV}$.

The dispersion was obtained from the electroluminescence spectrum via Kramers-Kronig transform. Although the measured spectrum shows a slight asymmetry due to inhomogeneous broadening, for simplicity we fit the gain spectrum to a Lorentzian line shape to obtain an analytical form for the dispersion. Any error in the dispersion will be small [17]. The relevant expressions are:

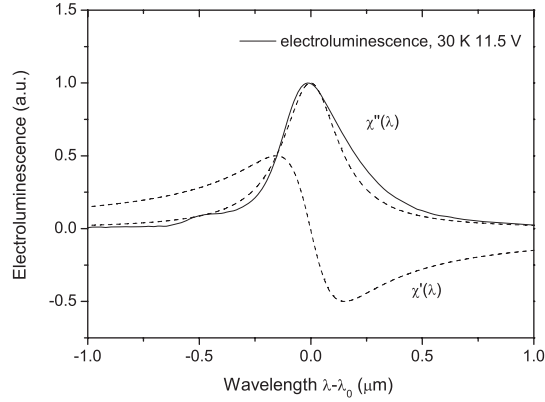


Fig. 7. Electroluminescence spectrum (D3281, solid line) without the laser cavity was measured at 30 K in order to determine the gain spectrum and thus the dispersion via the Kramers-Kronig relations. For simplicity, the spectrum was approximated by a Lorentzian line shape; the fit to the gain spectrum and the resulting dispersion are shown.

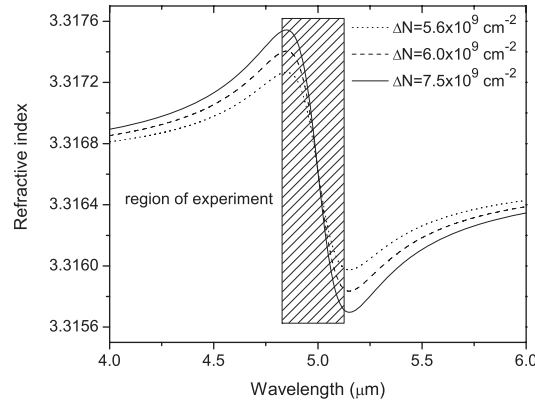


Fig. 8. Calculated refractive index based on the Eq. 8 is displayed for three different values of the population inversion ΔN .

$$\chi''(\nu) = \frac{e^2 z_{if}^2 \Delta N}{2\epsilon_0 \hbar} \frac{\Delta\nu/2\pi}{(\nu - \nu_0)^2 + (\frac{\Delta\nu}{2})^2} \quad (6)$$

$$\chi'(\nu) = \frac{e^2 z_{if}^2 (\omega_0 - \omega) T_2 \Delta N}{2\epsilon_0 \hbar} \frac{\Delta\nu/2\pi}{(\nu - \nu_0)^2 + (\frac{\Delta\nu}{2})^2} \quad (7)$$

where e is the elementary charge, z_{if} ($\simeq 1.65$ nm) is the calculated matrix element between the upper and lower lasing state, ΔN is the population inversion (to be determined below), ϵ_0 is the permittivity in free space, ν_0 (~ 5 μm) is the center emission frequency, T_2 is the total dephasing lifetime, and $\Delta\nu$ ($=1/\pi T_2$) is the corresponding FWHM (homogeneous broadening) of the lineshape function. T_2 is the sole free parameter required to fit the FWHM electroluminescence of Fig. 7, resulting in a value ~ 0.08 ps.

The index of refraction is related to the susceptibility of Eq. 6-7 by [18]

$$n = \text{Re}(\sqrt{\epsilon_b + \epsilon_0 \chi}) \quad (8)$$

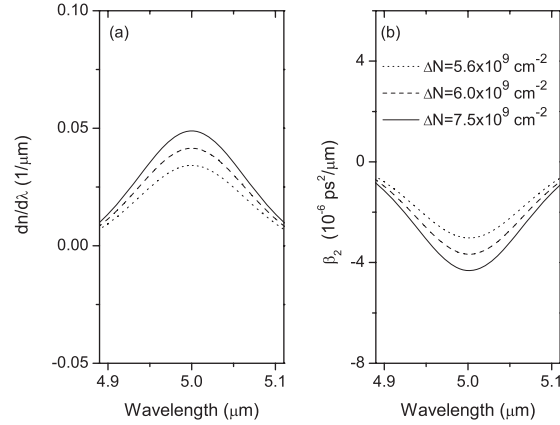


Fig. 9. Calculated index dispersion $dn/d\lambda$ and β_2 (using Eq. 4-5) only due to the small-signal gain are displayed in (a) and (b), respectively.

where ϵ_b ($\simeq 11$) is the background relative permittivity. Note that the frequency dependent complex permittivity is defined as $\epsilon(\omega) = \epsilon_b + \epsilon_0\chi(\omega)$, where χ is due to the intersubband transition. The refractive index is defined by $n = \text{Re} \sqrt{\epsilon(\omega)}$. The effect of differing population inversion is illustrated in Fig. 8. The dispersion due to the gain of course increases with population inversion. The contribution of the small-signal gain dispersion to the index dispersion and β_2 is summarized in Fig. 9.

5. Pulse broadening

In this section, we calculate the output pulse broadening based on linear dispersion theory using the value of β_2 obtained from the sum of material, waveguide, and gain dispersion, and compare the calculated (using Eq. 4-5) and observed group delay dispersion (Eq. 3) and pulse broadening. First, the sum of each dispersion component calculated in the previous sections was compared to the experimentally measured values. In Fig. 10(a), we show the calculated material and waveguide dispersion in section 3 as a dashed line. The gain dispersion from the electroluminescence spectrum in section 4 is displayed as a dotted line. In order to show the effect of small-signal gain, we showed β_2 for two different values of the population inversion ΔN . The sum of material, waveguide, and gain dispersion is shown as a solid line, whereas the experimentally measured values are shown as filled squares. As can be seen, the calculated total dispersion shows qualitatively good agreement with the measured data.

Given the value of β_2 , we then calculated the pulse broadening and compared with experimental to check self-consistency. Assuming no initial chirp on the injected mid-IR pulse, the input electric field can be approximated by a Gaussian envelope,

$$E_{in}(t, z = 0) = \exp\left(-2\ln 2 \frac{t^2}{\tau_{p0}^2}\right)$$

where the τ_{p0} is the intensity FWHM of the input pulse. The output pulse spectrum $E_{out}(w, z)$ can be obtained by multiplying the propagation factor $\exp(i\beta z)$ with the input pulse spectrum $E_{in}(w, z = 0)$. Taking the inverse Fourier transform of $E_{out}(w, z)$ back to the time domain, the

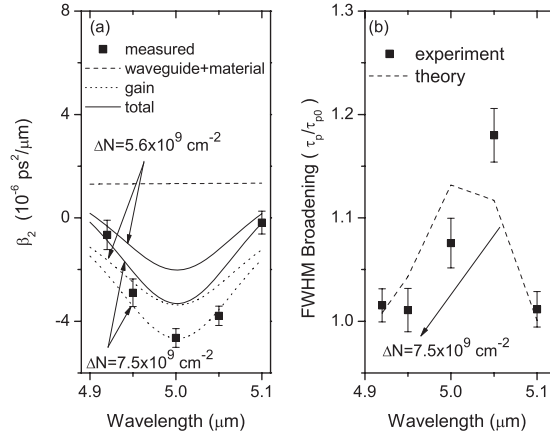


Fig. 10. (a) Contributions to the total GVD are separately displayed. Filled squares are the total β_2 ($=d^2\beta/d\omega^2$) from the upconversion measurements of Fig. 5(a). The material and waveguide dispersion (see Fig. 6) are shown as the dashed line, the gain dispersion (see Fig. 9) is as the dotted line, and total dispersion (sum of material, waveguide, and gain dispersion) is displayed as the solid line. (b) Corresponding pulse broadening, FWHM ratio τ_p/τ_{p0} , is displayed. Filled squares are from the upconversion measurements and dashed line is from the total GVD calculations.

intensity FWHM of the output pulse is obtained by using the following relations [19]:

$$\tau_p = \tau_{p0} \sqrt{1 + 4a_0^2 \beta_2^2 z^2}$$

$$, \tau_{p0} = \sqrt{\frac{2 \ln 2}{a_0}}$$

where τ_p is the intensity FWHM of the output pulse and z is the propagation distance, i.e. the QCL cavity length. In Fig. 10(b), we compare the measured and calculated pulse broadening as a function of wavelength given the obtained values of β_2 .

6. Conclusion

In conclusion, we report time-domain measurements of GVD in an active mid-IR QCL. The ultrafast upconversion technique based on sum-frequency generation was applied to investigate the GVD by measuring the wavelength-dependent pulse propagation delay, from which the estimated total GVD was in the negative dispersion regime and a maximum $\beta_2 \sim -4.6 \times 10^{-6} \text{ ps}^2/\mu\text{m}$ was observed at the $5 \mu\text{m}$ peak gain transition. The contributions of material and waveguide dispersion were calculated based on the detailed waveguide structures, and found to be comparatively small. The small-signal gain dispersion was isolated by an independent electroluminescence measurement without the laser cavity structure, confirming that the gain dispersion plays the most significant role in determining the overall GVD in the QCL active waveguide.

Acknowledgments

The authors would like to thank J. Faist for useful comments and discussion. The work at the University of Michigan is supported by the US Army Research Office. The Center for Nanoscale Systems (CNS) at Harvard University is also gratefully acknowledged. Harvard-CNS is a member of the National Nanotechnology Infrastructure Network (NNIN).